47th AIAA Aerospace Sciences Meeting and Exhibit, January 5–8, 2009/Orlando, FL

Effect of Wall Temperature and Mach Number on the Turbulence Structure of Hypersonic Boundary Layers

I. Beekman*, S. Priebe†, M. Ringuette‡and M. Pino Martín§

Department of Mechanical and Aerospace Engineering

Princeton University, Princeton, NJ 08544

The characterization of the turbulence structure using statistical analysis[1] and a geometric packet-finding algorithm[2] is explored. We follow structures which have been identified by the geometric packet-finding algorithm, using automated object segmentation and feature tracking software,[3,4] and observe how these structures and their associated wall signatures evolve in time. Using a direct numerical simulation database, we begin to assess the turbulence structure given by each method and the evolution of this structure.

I. Introduction

The coherence of the turbulence structure in boundary layers is now widely accepted. Theodorsen[5] postulated the existence of the hairpin vortex, a simple flow structure that explains the formation of low-speed streamwise streaks and the ejection of near-wall low-momentum fluid into higher-momentum regions farther from the wall, see Fig.1. Head & Bandyopadhyay[6] provided experimental evidence of the streamwise stacking of individual hairpin vortices into larger structures, packets, whose heads describe an envelope inclined at a 15° to 20° downstream angle. More recently, Adrian, Meinhart, & Tomkins[7] proposed a hairpin packet model, where the hairpins in a packet align in the streamwise direction as observed by Head and Bandyopadhyay. Packets enclose regions of low momentum induced by their heads and counter-rotating legs, and align themselves in the streamwise direction giving rise to the low-momentum, very large-scale motions (VLSM) observed experimentally by Jiménez[8] and Kim & Adrian,[9] see Fig.2. The current study of the turbulence structure in boundary layers has been confined largely to the subsonic flow regime (Tomkins & Adrian;[10] del Álamo & Jiménez;[11] Ganapathisubramani, Longmire & Marusic;[12] del Álamo *et al.*;[13] del Álamo *et al.*;[14] Guala, Hommena & Adrian;[15] Hambleton, Hutchins & Marusic;[16] Flores *et al.*;[17] Balakumar & Adrian;[18] Hutchins & Marusic[19] and Hutchins & Marusic,[20] for example).

The study of supersonic and hypersonic turbulent boundary layers has been primarily restricted to statistical analysis, due to the lack of detailed flow field data. Fernholz & Finley;[21] Fernholz & Finley;[22] Spina;[23] Smits & Wood;[24] Fernholz;[25] and Smits & Dussauge,[26] give reviews including the effects of pressure gradient, streamline curvature and the interaction with shock waves in high-speed turbulent boundary layers. These descriptions are statistical and some include qualitative flow visualizations. Structure information such as convection velocity, angle, and length scale, has been obtained from space-time correlations (see, for example, Smits *et al.*,[27] Spina,[28] and Smits & Dussauge[26]). The results indicate changes in structure properties with both Mach and Reynolds numbers, such as a decrease in structure length with increasing Mach number.

Recent advances in numerical and experimental techniques allow for detailed four-dimensional, in space and time, flow field data acquisition. Direct numerical simulations make possible the computation of turbulent boundary layers at supersonic and hypersonic Mach numbers (Guarini;[29] Martin;[30] Martin;[31] Pirozzoli & Grasso;[32] Xu & Martin;[33] Ringuette, Wu & Martin[2]) as well as the interaction of turbulence with strong,

*Student Member AIAA.

†Student Member AIAA.

‡Member AIAA.

§Assistant Professor, Senior Member pmartin@princeton.edu.

Case	M_∞	ρ_∞ (kg/m^3)	T_∞ (K)	T_w/T_∞	Re_θ	$\theta(mm)$	H	$\delta(mm)$
M3	2.99	0.0889	218.19	2.60	2328	0.423	5.1	5.69
M4	3.98	0.0914	219.20	3.84	3392	0.451	7.5	8.04
M5	4.96	0.0925	220.50	4.91	3669	0.388	9.5	8.90
M6	5.93	0.0942	221.86	7.30	4452	0.387	12.5	10.56
M7	6.88	0.0946	224.28	9.49	4990	0.374	15.4	12.11
M8	7.80	0.0948	227.72	11.91	5113	0.339	18.4	11.63
M5T2	5.00	0.0889	228.12	1.90	1691	0.190	7.4	3.20
M5T3	5.00	0.0908	224.12	2.39	2697	0.294	8.9	5.93
M5T4	5.00	0.0889	231.73	3.74	3713	0.443	10.1	8.92
M5T5	5.00	0.0937	220.97	5.40	5392	0.657	12.2	14.82

Table 1. Freestream, boundary layer, and wall parameters for the DNS.

Case	δ^+	L_x/δ	L_y/δ	L_z/δ	Δx^+	Δy^+	N_x	N_y	N_z
M3	297	9.6	2.4	15.7	7.5	2.8	384	256	106
M4	333	9.2	2.3	26.7	8.0	3.0	384	256	114
M5	318	9.7	2.4	25.1	8.1	3.0	384	256	110
M6	258	12.2	3.0	37.6	8.2	3.1	384	256	114
M7	228	9.0	2.5	30.8	8.1	3.0	256	192	109
M8	173	11.5	3.2	31.0	7.8	2.9	256	192	105
M5T2	378	7.9	2.0	15.8	7.8	3.0	384	256	110
M5T3	386	7.5	1.9	16.7	7.7	2.9	384	256	110
M5T4	368	7.8	1.9	16.4	7.5	2.8	384	256	110
M5T5	382	7.4	1.8	14.0	7.4	2.8	384	256	110

Table 2. Grid resolution and domain size for the DNS.

unsteady shock waves (Adams;[34] Pirozzoli & Grasso;[35] Wu & Martin;[36] Wu & Martin;[37] Taylor, Grube & Martin[38]). Advanced particle-image-velocimetry techniques allow the temporal and spatial characterization of experimental supersonic turbulent boundary layers and shock boundary layer interactions (Schrijer, Scarano & van Oudheusden;[39] van Oudheusden;[40] Humble, Scarano & van Oudheusden[41]). Both numerical[2,36] and experimental[42,43] data at supersonic Mach numbers have shown evidence of VLSM.

In this paper, we present a set of analytical tools to study the structures, in particular hairpin packets, and their wall signature in boundary layers. In Section II, we present the direct numerical simulation database of turbulent boundary layers with varying Mach number and wall-heat transfer. In Section III, we summarize the geometric algorithm that is used to identify packets, and the correlation analysis that is used to distinguish from weak, average and strong packets. We present preliminary results and conclusions in Sections IV and V respectively.

II. DNS Database

We use the DNS database of Martin,[30,31] extended to Mach 8. The nominal flow conditions are given in table 1, which provides the freestream density and temperature, ρ_∞ and T_∞, respectively, and the boundary layer properties: momentum thickness, θ, shape factor, $H = \delta^*/\theta$, where δ^* is the displacement thickness, Reynolds number based on θ, Re_θ, and boundary layer thickness δ. The wall condition for the Mach varying data is isothermal and prescribed to be nearly the adiabatic temperature. For each condition,we have accumulated 500 instantaneous DNS volumes, so that packet structures advance a total streamwise distance of about 70δ, however in the present work the analyses are performed over roughly 160. Re_θ is kept nearly

constant, with an insignificant variation across the cases, whereas δ^+ varies in roughly 175 to 400 across the cases. The domain size, L, and the number of grid points, N, for the simulations are given in table 2, with the ratio of δ to the wall unit, δ^+; the superscript $(^+)$ indicates scaling with inner, or wall values. We take the streamwise, spanwise, and wall-normal directions to be x, y, and z, respectively, and the grid resolutions in the streamwise and spanwise directions are denoted in table 2 as Δx^+ and Δy^+. The details of the numerical method are given by,[31] as well as the accuracy of the simulations as compared to theory and experiments. For reference, the DNS skin friction falls within 8% of the predictions.

III. Analytic Tools

A. Geometric Algorithm

The geometric algorithm is described in detail by Ringuette, Wu & Martin,[2] here we summarize it. The algorithm scans (x, z) planes for ideal packets conforming geometrically to the model of Adrian, Meinhart, & Tomkins.[7] Specifically, it searches for hairpin head, or transverse, vortices that are spaced close to one another ($\leq 0.5\delta$) in the streamwise direction and are arranged in a ramp-like formation with a small ($\leq 45°$) downstream angle relative to the wall. The head vortices are identified using a threshold of the spanwise vorticity, ω_y, and the swirling strength, λ_{ci},[44] such that λ_{ci} must be greater than or equal to $4.5\overline{\lambda_{ci}}$, where the over-bar indicates the mean, and ω_y is greater than or equal to 2 standard deviations from the mean; only the region between the buffer layer ($z^+ = 30$) and the boundary layer edge is considered for both computing the threshold quantities and finding hairpin packets. The current version of the algorithm implements a more sophisticated 'clustering' technique to find and catalog each vortex, where grid points flagged using the identification thresholds are considered to be part of a single structure with any other grid points if their grid locations are adjacent in any of the 8 planar directions. The algorithm has provisions for handling relatively large (wall-normal height $> 0.1\delta$, streamwise distance $> 0.1\delta$) structures that are occasionally identified by the thresholds, such as hairpin legs. The scheme checks whether or not a head vortex is above the leg, and does not consider the structure if no head is found. A further refinement of the algorithm, implemented in the current version, performs a least-squares-fit through the identified points of these large structures, and rejects the structure outright if the angle of the line is less than 25°. This removes the tendency of the algorithm to occasionally accept large, relatively horizontal shear layers with high ω_y or λ_{ci} as hairpin heads. The average packet properties determined using the algorithm before and after this improvement, however, show little change; the refinement is useful primarily for instantaneous visualizations.

For each DNS volume, statistics on packet properties are obtained from all (x, z) planes, and the results are averaged over multiple time realizations. Gathering packet statistics in two (x, z) planes separated by a spanwise distance of 0.75δ, so that the evaluated structures are entirely independent, produces results within 6% of the spanwise-averaged data. Properties such as the packet angle, length, and streamwise hairpin spacing, are based on the relative locations of the vortex cores in each packet. The geometric algorithm is useful for obtaining detailed packet statistics and generating instantaneous visualizations. Figure 3 plots contours of spanwise vorticity and velocity vectors identifying the hairpin heads that compose a packet in an instantaneous field of a Mach 3 boundary layer. Figure 4 plots iso-surfaces of swirling strength showing the three-dimensional visualization of the same packet.

B. Correlation Method

Brown & Thomas[1] identified the average large-scale coherent structure in the boundary layer associated with the unsteady signature of the wall shear stress, τ_w, by correlating τ_w at a single reference location with u at different wall-normal distances. Correlation profiles were constructed by varying the streamwise separation of u and τ_w, Δx, both by converting time into distance using Taylor's hypothesis of 'frozen convection' and physically shifting the streamwise measurement locations of u. They observed that the correlations peak at an increasing downstream distance with increasing wall-normal location, indicating a downstream-leaning coherent structure. Brown & Thomas[1] proposed that, if such a structure existed, then conditionally averaging the correlations on data traces that contained the structure would produce correlations of the same shape but with higher magnitudes, which they called 'enhanced' correlations. Their criterion used for the conditional averaging was that the correlation at $z/\delta = 0.25$ be greater than twice the peak value at the Δx location of the peak, indicating a 'strong' event such as a turbulent burst in the lower part of the boundary layer. Using this conditional method, they found stronger correlations of the same shape, which provided

evidence of a ramp-like coherent structure in the boundary layer.

We use the same method to identify the average coherent structure associated with strong events, and find it to have the characteristics of a hairpin packet. For each DNS condition, we perform the correlation between τ_w and ρu at a streamwise location, x, as follows:

$$R_{\tau_w(\rho u)}(\Delta x) = 1/(x_2 - x_1) \left\langle \overline{\int_{x_1}^{x_2} \tau'_w(x)(\rho u)'(x + \Delta x)dx} \right\rangle / \tau'_{w,RMS}(\rho u)'_{RMS}.$$

The over-bar and angle brackets denote spatial (streamwise and spanwise) and temporal averaging, respectively. A streamwise correlation width of $-2\delta \leq \Delta x \leq 4\delta$ was sufficient for both the average and 'enhanced' correlations to fall below 0.2. The correlation is done with mass-flux data at eleven wall-normal grid locations, starting with $z/\delta = 0.05$ and $z/\delta = 0.1$, then proceeding in 0.1δ increments to the boundary layer edge. The 'enhanced' correlation is performed as described above, using the peak value and location of the average correlation at $z/\delta = 0.2$; the RMS values used to normalize this correlation are those of the strong events. Figure 5 plots the Average and enhanced correlations for the Mach 3 data. Using this technique, we can condition the sampling of the data and distinguish between weak, average and strong packets.

C. Relationship between the Geometric Algorithm and the Correlation Method

We determine profiles of the convection velocity for vortices belonging to hairpin packets using both the geometric algorithm and the 'enhanced' correlation data. For the geometric algorithm,the convection velocity of a single vortex in a packet is computed by averaging u at each grid point within the vortex; the value is then associated with a wall-normal location corresponding to the vortex core, assumed to be where λ_{ci} for the vortex is a maximum. Although gathering statistics in two (x, z) planes is sufficient for determining the average packet properties, more samples are required for converged profiles of the packet convection velocity. To obtain further samples, we used the packet-finding code to identify packet vortices in every (x, z) plane (i.e. the entire DNS volume), then employed a simple algorithm to scan through the volume and gather convection velocity data only from purely independent vortices. The algorithm first finds a packet vortex in a single (x, z) plane, computes the convection velocity of this vortex as described above, and then removes from consideration all other vortex grid points within a $(-0.15 \leq \Delta x/\delta \leq 0.15) \times (-0.5 \leq \Delta y/\delta \leq 0.5) \times (-0.15 \leq \Delta z/\delta \leq 0.15)$ volume centered on the original point. The spanwise distance of 0.5δ is approximately the average packet width, while the average streamwise packet vortex spacing is about 0.15δ at all Mach numbers. This conservative spatial separation between data points provides statistical samples that are clearly from independent structures. However, the results are very similar to those obtained using every packet vortex in every (x, z) plane (i.e. spanwise averaging of the planar data).

For the 'enhanced' correlation method, we obtain the packet convection velocity at the eleven wall-normal distances by computing the correlation profiles between u and the shear stress at each (x, y) wall location (no spanwise or streamwise averaging). If the correlation peak at $z/\delta = 0.2$ indicates a 'strong' event, the streamwise velocity u is sampled at the $(x + \Delta x, z)$ peak location of the correlation profile at each of the eleven wall-normal distances. The results at each z-location are averaged together. The $(x + \Delta x, z)$ peak locations can be thought of as lying within the back of the ramp-like structure associated with each instantaneous strong event. We chose to present the 'enhanced'-correlation and geometric-algorithm data spanwise averaged over all planes.

Essentially, statistics on the average packet structure can be found using the correlation analysis of Brown and Thomas and the data can be categorized into average-strong, average-average, and average-weak packets. In contrast, the geometric algorithm identifies only the subset of packets that conforms with an ideal geometric criteria. When the geometric analysis is combined with the correlation analysis, the geometric events can be also decomposed into average strong-geometric, average-geometric, and weak-geometric packets.

Figure 6 plots the averaged vortex convection velocity and the mean flow velocity profiles for the Mach 3 data, given by the geometric analysis combined with the correlation analysis. For reference, the average convection velocity of strong packets given solely by the correlation analysis is also plotted, as well as the mean velocity profile. The data suggest that the average geometric packet is representative of strong statistical packets.

D. Packet Tracking

We use the Object Segmentation and Feature Tracking (Ostrk2.0) software package[3,4] to identify individual vortical structures and track their evolution through subsequent flow realizations. The tracking software operates on a set of subsequent, instantaneous, three-dimensional fields of the swirling strength. Ostrk 2.0 performs two distinct tasks on these data. First, it extracts vortical structures from the instantaneous swirling strength fields. This is the object segmentation part of the software. The vortical features are identified based on an iso-surface of the swirl that is generated at a user-specified threshold level (we use a threshold of $4.5\overline{\lambda_{ci}}$). Once the vortical structures have been identified in each individual flow realization, their evolution is tracked through time from one flow realization to the next. The tracking algorithm recognizes the creation of new objects, the merging of objects as well as the split and dissipation of objects. Further details on Ostrk2.0, including the algorithms used for object segmentation and feature tracking, can be found in the User Manual by Liang,[3] and the paper by Wang and Silver.[4]

O'Farrell and Martin[45] find that the tracking software performs poorly on a Mach 3 turbulent boundary layer. When tracking an individual structure, or a small group of structures, the tracking software mistakenly identifies a rapidly growing number of neighboring objects as belonging to the original structure. In other words, the tracking software 'proliferates' the original structure. In order to eliminate this shortcoming, we perform a number of pre-processing operations on the swirling strength fields. These pre-processing operations are physically-rooted. First, we use the packet finding algorithm described in section A above to identify geometrically-ideal hairpin packets. Second, we discard all hairpin packets except for those that are associated with 'strong' events at the wall. By a 'strong' event, we mean a region at the wall where the Brown and Thomas correlation, which was introduced in section B above, is elevated. The field that is used for tracking contains the 'strong', geometrically-ideal hairpin packets only. At all points that do not belong to one of these hairpin packets, the swirling strength is set to zero in these fields.

Figure 7 illustrates the tracking of a hairpin packet in a Mach 3, $Re_\theta = 2,390$ turbulent boundary layer. An iso-surface of the swirling strength corresponding to $4.5\overline{\lambda_{ci}}$ is shown, with the selected hairpin appearing in blue. We show four subsequent time realizations to illustrate the tracking of the hairpin and its evolution over time.

Figure 8 shows a canonical hairpin packet (visualized by an iso-surface of swirl) in incompressible channel flow. The simulation was started with a single, ideal hairpin vortex. At the later time shown in figure 8 this single hairpin vortex has spawned a child vortex at its upstream end. The entire hairpin packet, composed of the child and parent objects, was successfully tracked with Ostrk2.0.

E. Wall Signatures

The experiments of Brown and Thomas,[1] and Thomas and Bull[46] in incompressible boundary layers have shown characteristic patterns in the wall-shear stress and wall-pressure, which are hypothesized to be associated with large-scale coherent motions. Figure 9 is a reproduction of a schematic from the paper by Thomas and Bull,[46] which shows a large-scale, coherent motion together with the associated wall shear stress and pressure signatures. Figure 10 shows the canonical case of a single, isolated hairpin vortex in incompressible channel flow. The hairpin vortex is visualized in a streamwise-spanwise plane and in a streamwise-wall normal plane using an iso-surface of the swirl at 10% of the maximum swirl value for the initial frame in the data set. The wall shear stress signature and the wall-pressure signature sampled at y = 2.97δ are also shown. Due to its simplicity, this canonical flow is useful for verifying the hypothesized wall signatures of hairpin packets. It is apparent that the shear stress has a peak at a location that coincides with the downstream end of the hairpin legs. The wall-pressure distribution, however, has a significant minimum at a location that coincides with the intersection of the hairpin head and its legs.

IV. Preliminary Results

A. General Effect on the Turbulence

We first examine how varying Mach number and wall temperature affect the transport of turbulence. Some of the dynamics of the near-wall transport mechanisms may be observed from the turbulent kinetic energy budget. There are four mechanisms for the exchange of turbulent kinetic energy: turbulent transport,

production, dissipation and viscous diffusion. The budget equation for the turbulent kinetic energy is

$$\frac{\partial}{\partial t}\left(\overline{\rho}\widetilde{k}\right) + \widetilde{w}\frac{\partial}{\partial z}\left(\overline{\rho}\widetilde{k}\right) = P + T + \Pi_t + \Pi_d + \phi_{dif} + \phi_{dis} + ST$$

where

$$\begin{aligned}
P &= -\overline{\rho u_i'' w''}\frac{\partial \widetilde{u}_i}{\partial z}, \\
T &= -\frac{1}{2}\frac{\partial}{\partial z}\overline{\rho u_i'' u_i'' w''}, \\
\Pi_t &= -\frac{\partial}{\partial z}\overline{w'' p'}, \qquad\qquad \Pi_d = \overline{p'\frac{\partial u_i''}{\partial x_i}}, \\
\phi_{dif} &= \frac{\partial}{\partial z}\overline{u_i'' \sigma_{i2}'}, \qquad\qquad \phi_{dis} = \overline{\sigma_{ij}'\frac{\partial u_i''}{\partial x_j}} \\
ST &= -\overline{w''}\frac{\partial \overline{p}}{\partial z} + \overline{u_i''}\frac{\partial \overline{\sigma_{ij}}}{\partial x_j} - \overline{\rho}\,\overline{k}\,\frac{\partial \widetilde{w}}{\partial z},
\end{aligned}$$

and P is the turbulent energy produced due to mean gradients, T is the turbulent transport of kinetic energy, Π_t is the diffusion due to pressure, Π_d is the pressure dilation term, ϕ_{dif} is the viscous diffusion term, ϕ_{dis} is the viscous dissipation term, and ST represents a group of small terms. The first two of these are due to the difference between Favre and Reynolds averaging and the third is a dilation-production term.

These terms are normalized by inner units and plotted in Figure 11 for the wall temperature varying data and Figure 12 for the Mach number varying data. As expected, these terms reach their maximum values within the buffer layer and attenuate with increasing wall-normal distance. Figure 11(a)–11(e) plot each term individually for the varying wall temperature data versus z^+. All these terms are combined in Figure 11(f) and plotted against ζ^+. ζ^+ is a coordinate transform that takes into account mean variations of the thermodynamic variables and molecular transport coefficients across the boundary layer to collapse the data. It is given by

$$\zeta^+ = \int_0^z \frac{\langle\rho\rangle u_\tau}{\langle\mu\rangle} dz.$$

The maximum and minimum wall-normal locations of the budget terms are roughly the same when plotted against ζ^+, where as their locations do not collapse when plotted against z^+. We find that the magnitudes of these budget terms are attenuated as the wall temperature is lowered. This is consistent with the notion that a cooled wall acts as an energy sink, removing available energy from the flow. Figure 11(f) shows all of the dominant budget terms plotted against z^+ for the varying Mach number simulations. We observe little difference in these budget terms between the various Mach numbers, other than a slight increase in the production and dissipation terms with increasing Mach number.

B. Packet Geometry and Convection Velocities

From the correlations of τ_w and ρu we can find the hairpin packet geometry and average downstream leaning angle of packets. A set of points may be determined by finding the Δx locations where the correlation coefficient reaches its maximum at different wall-normal distances. A least squares linear regression may be applied to these points to determine the characteristic structure angle. This may be done for 'strong,' 'average,' and 'weak' correlations and may be done with the additional requirement that a 'geometric event' at the wall is present. This 'geometric event' is found by performing a least squares linear regression on the points located at hairpin vortex cores, within a given packet, and finding where it intersects with the wall. In Figure 13 we observe the geometry and, qualitatively, the characteristic angle and the ramp like structures, but note that the data are poorly converged.

We are similarly able to obtain packet convection velocities by finding the mean of the velocities at each wall-normal location where the instantaneous correlation, $R_{\tau(\rho u)}$, is at a maximum. 'Strong' and 'weak' events may be distinguished in the same manner that the conditional method of Brown and Thomas[1] is taken: velocities are sampled at each wall-normal location when the instantaneous correlation at $z/\delta = 0.2$ indicates a strong or a weak event. Figures 14(a–c) show the 'strong,' 'average,' and 'weak' convection velocities using only the statistical correlation method. Figures 14(d–f) show the convection velocities with

the further condition that a geometric event is present at the wall. The mean velocity profiles are included for reference. As expected the 'strong' packets induced greater drag and are the slowest whereas the 'weak' packets convect approximately with the mean flow and in the Mach 7 and 8 cases even more quickly. It is interesting that the profiles of average convection velocities of statistically strong packets, Figure 14(a), and that of ideal geometric packets, Figure 14(e), are nearly identical. This seems to suggest that ideal geometric packets are representative of strong events across the Mach varying data.

C. Packet Tracking and Wall Signatures

We have successfully tracked a hairpin packet using the Ostrk software discussed in section III D. Using this software we have followed a hairpin packet, highlighted in red in Figure 15, in a Mach 8 flow. After tracking this packet and watching it evolve in time, we have plotted the associated wall signatures at a selected instance in time. Figure 16 shows the wall pressure signature and Figure 17 shows the wall shear stress signature. Above each of these wall signature plots is a visualization, using iso-surfaces of the swirl at $4.5\overline{\lambda_{ci}}$, for the hairpin packet that we have identified and isolated. Two views of this packet are presented, one looking down in the wall-normal direction and one from the side looking in the spanwise direction. The structure of the hairpins in this particular packet is cane like, with multiple sets of counter rotating legs, or canes. Both wall signatures are pronounced, and there is a significant peak in the wall shear stress associated with the tail of the hairpin legs, as was observed for the lone hairpin in incompressible channel flow, shown in Figure 10, and as hypothesized by Brown & Thomas and Thomas and Bull.

V. Summary

We have presented a number of analytic tools and techniques for identifying, quantifying, characterizing, and tracking the evolution of hairpin packets. The geometric algorithm described in section A is used to identify ideal hairpin packets conforming geometrically to the model of Adrian, Meinhart, and Tomkins.[7] We have also repeated the analysis of Brown and Thomas[1] to further investigate the large scale coherent motions. Additionally, using the 'geometric events' at the wall we may perform the Brown and Thomas statistical correlation analysis on a subset of the data identified as hairpin packets by the geometric algorithm. From these analyses we are able to find basic statistical quantities, such as the characteristic structure angle, packet convection velocities, and information about the size, strength, and number of hairpin vortices making up these packets.

Additionally, using the Ostrk2.0 object segmentation and feature tracking software,[3,4] we are able to track hairpin packets identified by the geometric algorithm, which are associated with 'strong' events at the wall. Through this we have an automated means of observing the evolution of hairpin packets and their associated wall signatures.

Some rough, preliminary results associated with these analyses have been presented in section IV. We note that these analyses have only been performed using a subset of the data which is now available to us. When utilizing the entire data set, the convergence of the results presented in section IV, especially that of the packet geometries (Figure 13), is expected to improve. In the future we plan to continue to use these tools across the entire data set, and continue to present our findings on the effect of heat transfer and Mach number on the structure of turbulent boundary layers.

VI. Acknowledgments

This work is sponsored by the Air Force Office of Scientific Research under Grant AF/9550-06-1-0323 and NASA under Grant NNX08AD04A.

References

[1]Brown, G. L. and Thomas, A. S. W., "Large structure in a turbulent boundary layer," *Phys. Fluids*, Vol. 10, No. 2, 1977, pp. 243–251.

[2]Ringuette, M. J., Wu, M., and Martín, M. P., "Coherent structures in direct numerical simulation of turbulent boundary layers at Mach 3," *J. Fluid Mech.*, Vol. 594, 2008, pp. 59–69.

[3]Liang, L., "User Manual for Object-Segmentation and Feature-Tracking (ostrk2.0) Using AVS/exp Package," Tech. rep., Rutgers, The State University of New Jersey, 2003.

[4]Wang, X. and Silver, D., "Tracking and Visualizing Turbulent 3D Features," *IEEE Transactions on on Visualization and Computer Graphics*, Vol. 3, No. 2, 1997, pp. 129–141.

[5]Theodorsen, T., "Mechanism of Turbulence," *Proc. 2nd. Midwestern Conf. on Fluid Mech.*, Ohio State University, Columbus, Ohio, USA, 1952, pp. 1–19.

[6]Head, M. and Bandyopadhyay, P., "New aspects of turbulent boundary-layer structure," *J. Fluid Mech.*, Vol. 107, 1981, pp. 297–338.

[7]Adrian, R., Meinhart, C., and Tomkins, C., "Vortex organization in the outer region of the turbulent boundary layer," *J. Fluid Mech.*, Vol. 422, 2000, pp. 1–54.

[8]Jiménez, J., "The largest scales of turbulent wall flows," *Center for Turbulence Research, Annual Research Briefs*, Stanford University, 1998, pp. 137–154.

[9]Kim, K. C. and Adrian, R. J., "Very large-scale motion in the outer layer," *Phys. Fluids*, Vol. 11, No. 2, 1999, pp. 417–422.

[10]Tomkins, C. and Adrian, R., "Spanwise structure and scale growth in turbulent boundary layers," *J. Fluid Mech.*, Vol. 490, 2003, pp. 37–74.

[11]del Álamo, J. C. and Jiménez, J., "Spectra of the very large anisotropic scales in turbulent channels," *Phys. Fluids*, Vol. 15, No. 6, 2003, pp. L41–L44.

[12]Ganapathisubramani, B., Longmire, E. K., and Marusic, I., "Characteristics of vortex packets in turbulent boundary layers," *J. Fluid Mech.*, Vol. 478, 2003, pp. 35–46.

[13]del Álamo, J. C., Jiménez, J., Zandonade, P., and Moser, R. D., "Scaling of the energy spectra of turbulent channels," *J. Fluid Mech.*, Vol. 500, 2004, pp. 135–144.

[14]del Álamo, J. C., Jiménez, J., Zandonade, P., and Moser, R. D., "Self-similar vortex clusters in the turbulent logarithmic region," *J. Fluid Mech.*, Vol. 561, 2006, pp. 329–358.

[15]Guala, M., Hommema, S. E., and Adrian, R. J., "Large-scale and very-large-scale motions in turbulent pipe flow," *J. Fluid Mech.*, Vol. 554, 2006, pp. 521–542.

[16]Hambleton, W. T., Hutchins, N., and Marusic, I., "Simultaneous orthogonal-plane particle image velocimetry measurements in a turbulent boundary layer," *J. Fluid Mech.*, Vol. 560, 2006, pp. 53–64.

[17]Flores, O., Jiménez, J., and del Álamo, J. C., "Vorticity organization in the outer layer of turbulent channels with disturbed walls," *J. Fluid Mech.*, Vol. 591, 2007, pp. 145–154.

[18]Balakumar, B. J. and Adrian, R. J., "Large- and very-large-scale motions in channel and boundary-layer flows," *Phil. Trans. R. Soc. A*, Vol. 365, 2007, pp. 665–681.

[19]Hutchins, N. and Marusic, I., "Evidence of very long meandering features in the logarithmic region of turbulent boundary layers," *J. of Fluid Mechanics*, , No. 579, 2007, pp. 1–28.

[20]Hutchins, N. and Marusic, I., "Large-scale influences in near-wall turbulence," *Phil. Trans. R. Soc. A*, Vol. 365, 2007, pp. 647–664.

[21]Fernholz, H. H. and Finley, P. J., "A critical commentary on mean flow data for two-dimensional compressible turbulent boundary layers," *AGARDograph 253*, 1980.

[22]Fernholz, H. H. and Finley, P. J., "A further compilation of compressible turbulent boundary layer data with a surveyof turbulence data," *AGARDograph 263*, 1981.

[23]Spina, E., Smits, A., and Robinson, S., "The physics of supersonic turbulent boundary layers," *J. Fluid Mech.*, Vol. 26, 1994, pp. 287–319.

[24]Smits, A. and Wood, D., "The response of turbulent boundary layers to sudden perturbations," *Annual Review of Fluid Mechanics*, Vol. 17, 1985, pp. 321–358.

[25]Fernholz, H. H., Smits, A., Dussauge, J., and Finley, P., "A survey of measurements and measuring techniques in rapidly distorted compressible turbulent boundary layers," *AGARDograph 315*, 1989.

[26]Smits, A. J. and Dussauge, J.-P., *Turbulent shear layers in supersonic flow*, Springer, 2nd ed., 2006.

[27]Smits, A., Spina, E., Alving, A., Smith, R., Fernando, E., and Donovan, J., "A comparison of the turbulence structure of subsonic and supersonic boundary layers," *Phys. Fluids A*, Vol. 1, 1989, pp. 1865–1875.

[28]Spina, E., Donovan, J., and Smits, A., "On the structure of high-Reynolds number supersonic turbulent boundary layers," *J. Fluid Mech.*, Vol. 222, 1991, pp. 293–327.

[29]Guarini, S., Moser, R., Shariff, K., and Wray, A., "Direct numerical simulation of supersonic turbulent boundary layer at Mach 2.5," *Journal of Fluid Mechanics*, Vol. 414, 2000, pp. 1–33.

[30]Martín, M. P., "DNS of hypersonic turbulent boundary layers," *AIAA Paper 2004-2337*, 2004.

[31]Martín, M. P., "Direct numerical simulation of hypersonic turbulent boundary layers. Part 1: initialization and comparison with experiments," *J. Fluid Mech.*, Vol. 570, 2007, pp. 347–364.

[32]Pirozzoli, S., Grasso, F., and Gatski, T., "Direct numerical simulation and analysis of a spatially evolving supersonic turbulent boundary layer at M=2.25," *Phys. Fluids*, Vol. 16, No. 3, 2004, pp. 530 – 545.

[33]Xu, S. and Martín, M., "Assessment of Inflow Boundary Conditions for Compressible Turbulent Boundary Layers," *Physics of Fluids*, Vol. 16, No. 7, 2004, pp. 2623–2639.

[34]Adams, N., "Direct simulation of the turbulent boundary layer along a compression ramp at $M = 3$ and $Re_\theta = 1685$," *Journal of Fluid Mechanics*, Vol. 420, 2000, pp. 47–83.

[35]Pirozzoli, S. and Grasso, F., "Direct numerical simulation of impinging shock wave/turbulent boundary layer interaction at M=2.25," *Phys. Fluids*, Vol. 18, No. 6, 2006.

[36]Wu, M. and Martín, M., "Direct numerical simulation of shockwave and turbulent boundary layer induced by a compression ramp," *AIAA J.*, Vol. 45, 2007, pp. 879–889.

[37]Wu, M. and Martín, M., "Analysis of shock motion in shockwave and turbulent boundary layer interaction using direct numerical simulation data," *J. of Fluid Mechanics*, Vol. 594, 2008, pp. 71–83.

[38]Taylor, E. M., Grube, N., and Martín, M. P., "Evaluation of traditional and shock-confininf LES filters using data of compressible turbulence," *AIAA Paper Number 2007-4197*, 2007.

[39]Schrijer, F., Scarano, F., and van Oudheusden, B., "Application of PIV in a Mach 7 double-ramp flow," *Experiments in Fluids*, Vol. 41, 2006, pp. 353–363.

[40]van Oudheusden, B., "Principles and application of velocimetry-based planar pressure imaging in compressible flows with shocks," *Experiments in Fluids (electronic Open Access)*, 2008.

[41]Humble, R., Scarano, F., and van Oudheusden, B., "Experimental study of an incident shock wave/turbulent boundary layer interaction using PIV," *AIAA Paper Number*, Vol. number 2006-3361, 2006.

[42]Ganapathisubramani, B., Clemens, N., and Dolling, D., "Large-scale motions in a supersonic turbulent boundary layer," *J. Fluid Mech.*, Vol. 556, 2006, pp. 1–11.

[43]Ganapathisubramani, B., Clemens, N., and Dolling, D., "Effects of upstream boundary layer on the unsteadiness of shock-induced separation," *J. Fluid Mech.*, Vol. 585, 2007, pp. 369–394.

[44]Zhou, J., Adrian, R., Balachandar, S., and Kendall, T., "Mechanisms for generating coherent packets of hairpin vortices in channel flow," *J. Fluid Mech.*, Vol. 387, 1999, pp. 353–396.

[45]O'Farrell, C. and Martin, M., "Chasing Eddies and Their Wall Signature in DNS Data of Turbulent Boundary Layers," *submitted to Journal of Turbulence*, 2008.

[46]Thomas, A. S. W. and Bull, M. K., "On the role of wall-pressure fluctuations in deterministic motions in the turbulent boundary layer," *J. Fluid Mech.*, Vol. 128, 1983, pp. 283–322.

[47]Green, M. A., Rowley, C. W., and Haller, G., "Detection of Lagrangian Coherent Structures in three-dimensional turbulence," *J. Fluid Mech.*, Vol. 572, 2007, pp. 111–120.

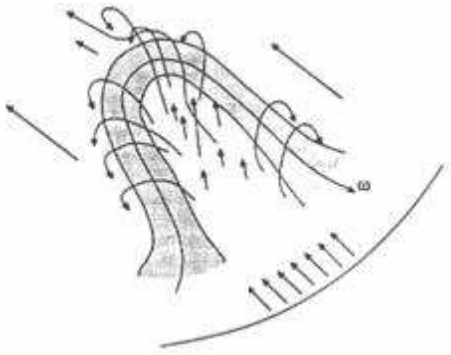

Figure 1. Theodorsen's hairpin vortex.[5] The arrows on either side of the hairpin indicate the direction of the flow.

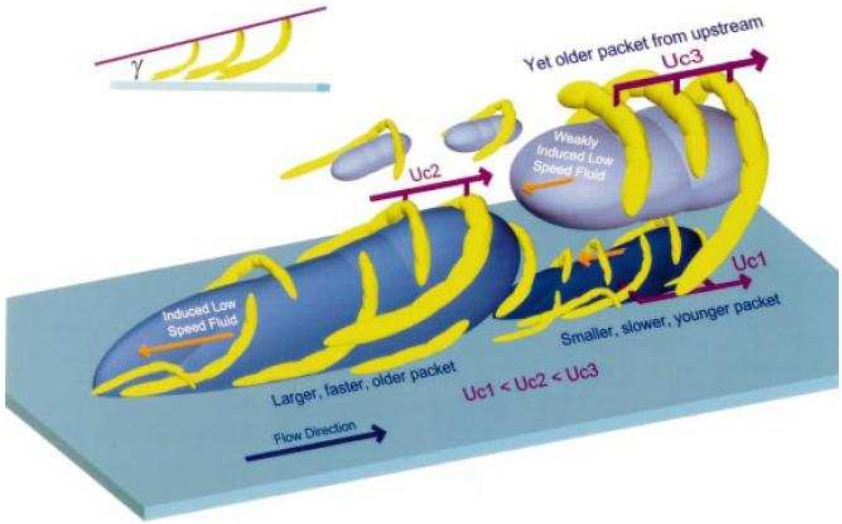

Figure 2. Hairpin packet model of Adrian *et al.*[7].

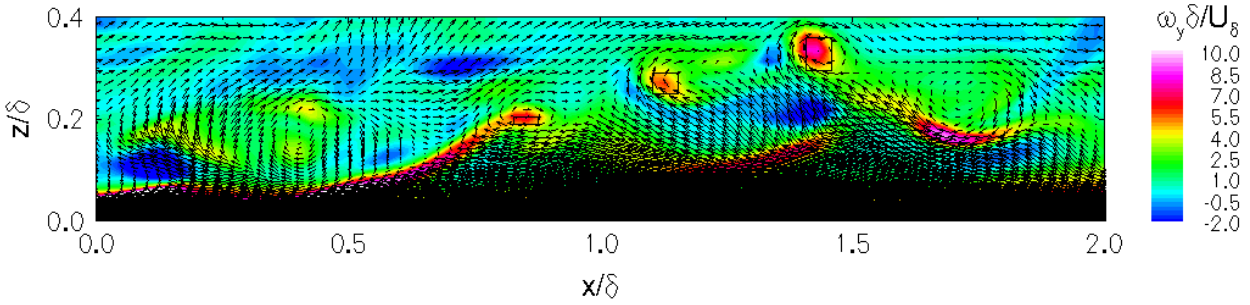

Figure 3. An x-z slice showing a hairpin packet from Ringuette *et al.*[2] (flow from left to right). Contours show spanwise vorticity and vectors give the in-plane velocity with $0.69U_\delta$ subtracted from u. The black boxes mark the hairpin heads identified by their packet finding algorithm.

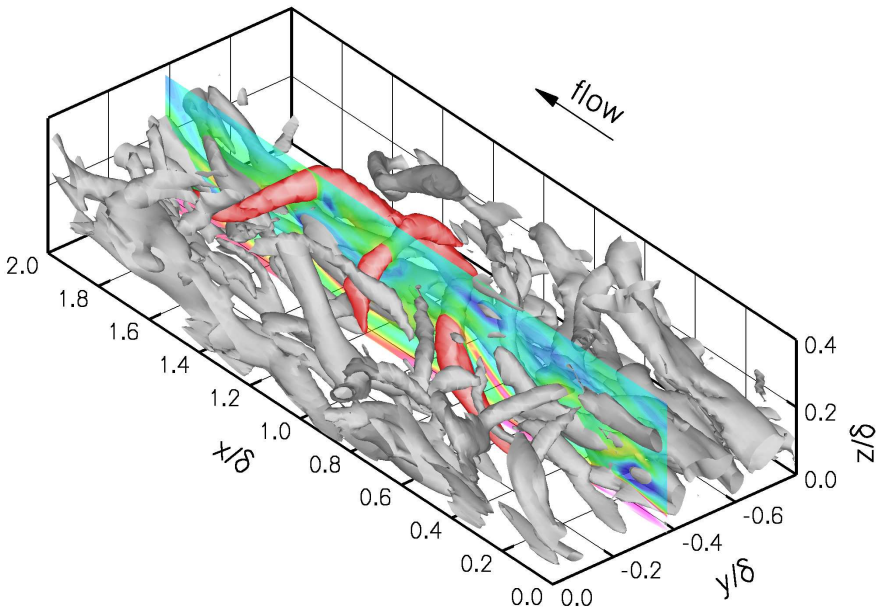

Figure 4. Hairpin packet visualization using iso-surfaces of swirling strength from Ringuette *et al.*[2] The hairpins identified in Figure 3 are highlighted in red.

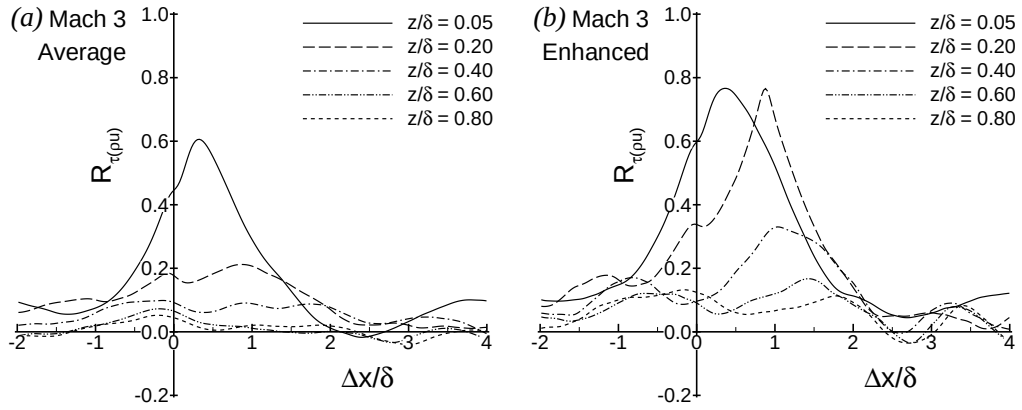

Figure 5. Spatial correlations between τ_w and ρ_u versus streamwise distance at different wall-normal locations at Mach 3. Figure 5(a): 'average' correlations; Figure 5(b): 'enhanced' correlations.

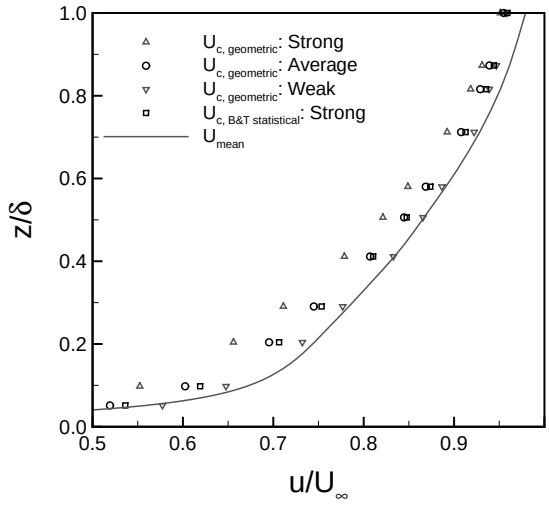

Figure 6. Mach 3 vortex convection velocity profiles, with the mean velocity profile as a solid line. The use of the 'geometric events' at the wall limit the correlational analysis to regions where ideal hairpin packets have been found, which correspond to the first three legend entries. The convection velocity determined from the 'strong' Brown and Thomas correlation[1] is plotted as a square symbol and is quite close in magnitude to the 'average' geometric convection velocity.

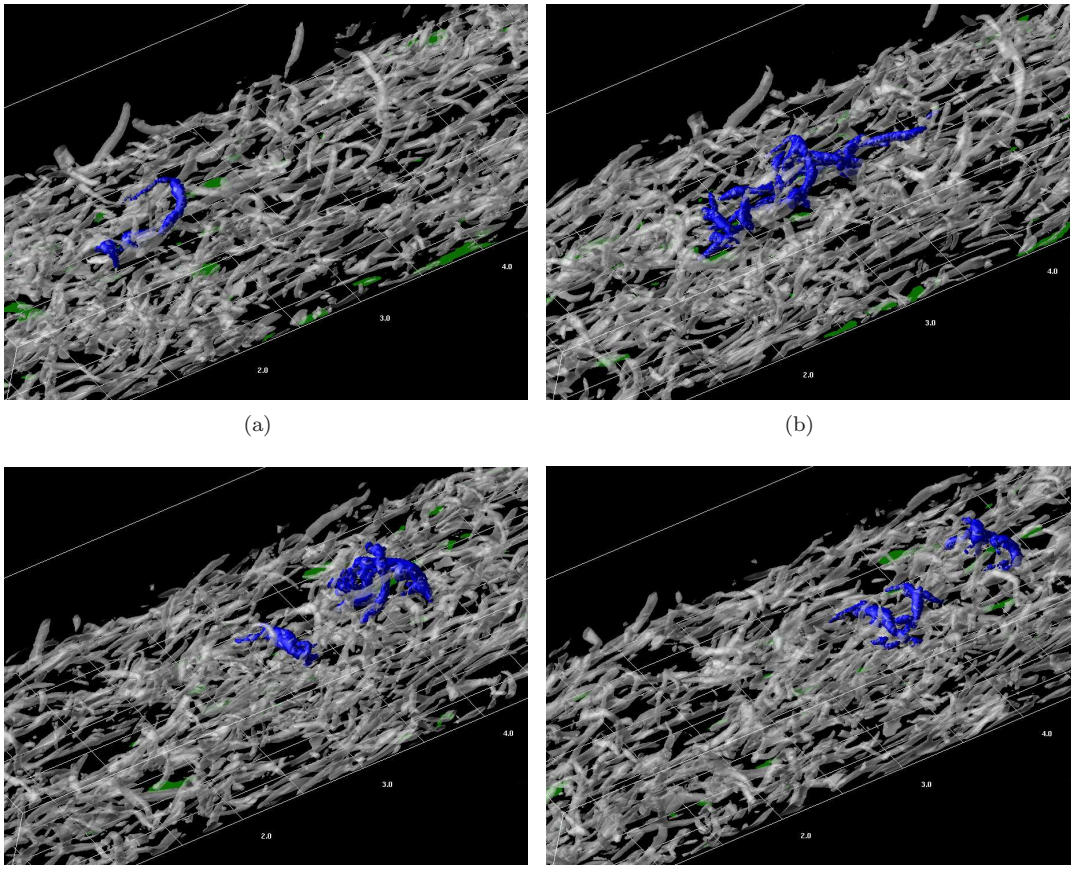

(a) (b)

(c) (d)

Figure 7. Tracking hairpin packet in a Mach 3 boundary layer at $Re_\theta = 2,390$. A hairpin packet was identified in 7(a) and highlighted in blue. All other vortices are shown in white and at 50% translucency. The packet was then tracked through subsequent DNS frames.

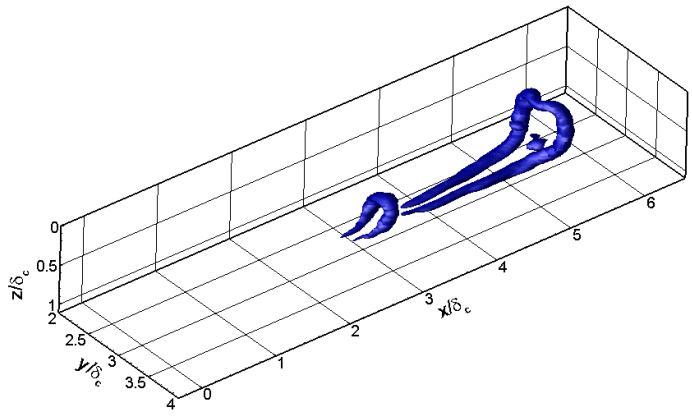

Figure 8. Iso-surfaces of swirling strength of a single hairpin vortex spawning another one to form a packet. Child and parent objects successfully tracked using the feature tracking and segmentation software. Data taken from a DNS of incompressible channel flow by Green *et al.*[47].

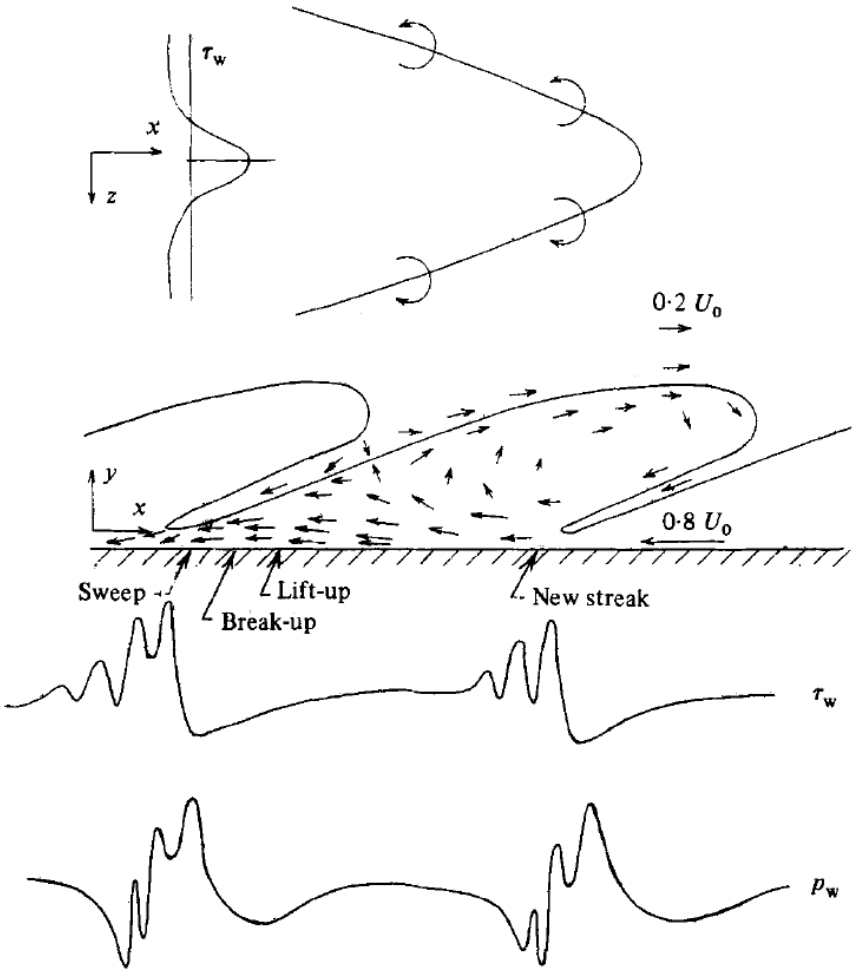

Figure 9. Model of organized structures in turbulent boundary Layers from Thomas & Bull,[46] after Brown & Thomas,[1] as seen by an observer moving at $0.8U_0$

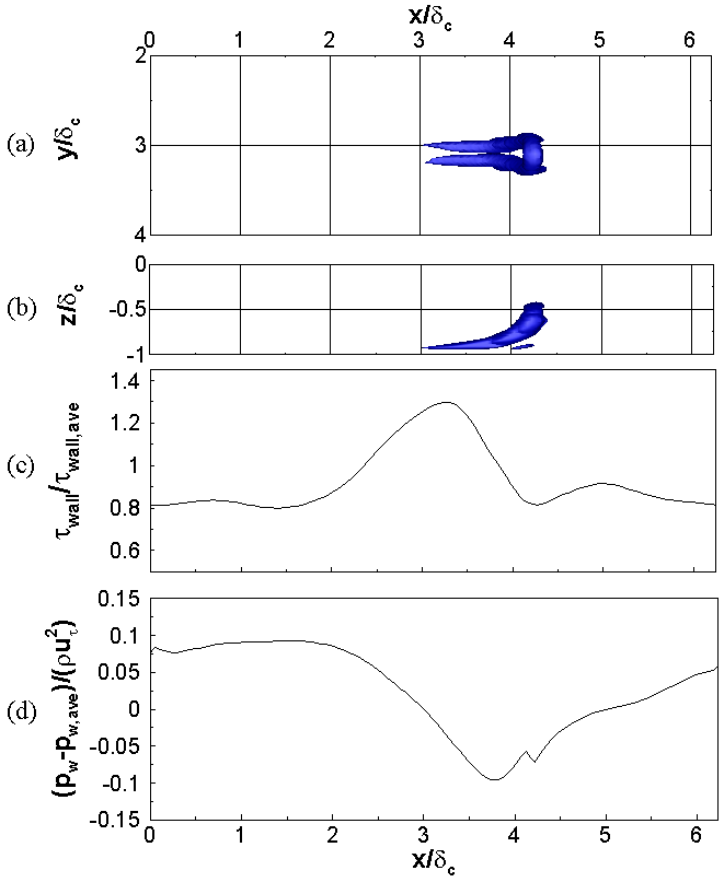

Figure 10. Wall signatures in τ_{wall} and p_{wall} for a lone hairpin packet in incompressible channel flow. Data taken from a DNS of incompressible channel flow by Green *et al.*[47].

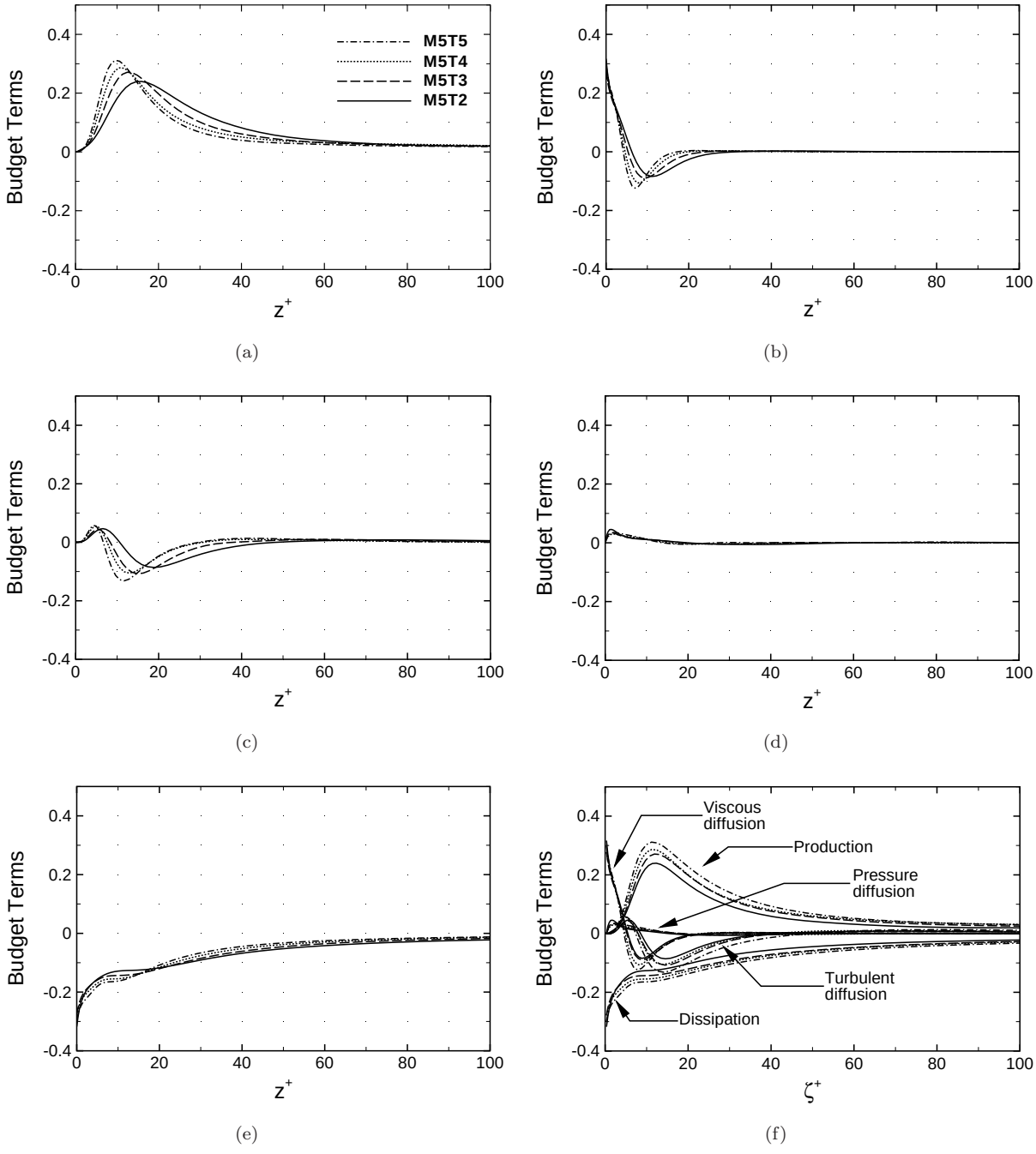

Figure 11. Turbulent kinetic energy budgets for the wall temperature varying data. Each term is non-dimensionalized with $u_\tau \tau_w / z_\tau$ where $\tau_w = \rho_w u_\tau^2$. (*a*–*e*) Individual terms of the wall temperature varying data plotted against z^+. (*f*) All the terms of the wall temperature varying data plotted against ζ^+.

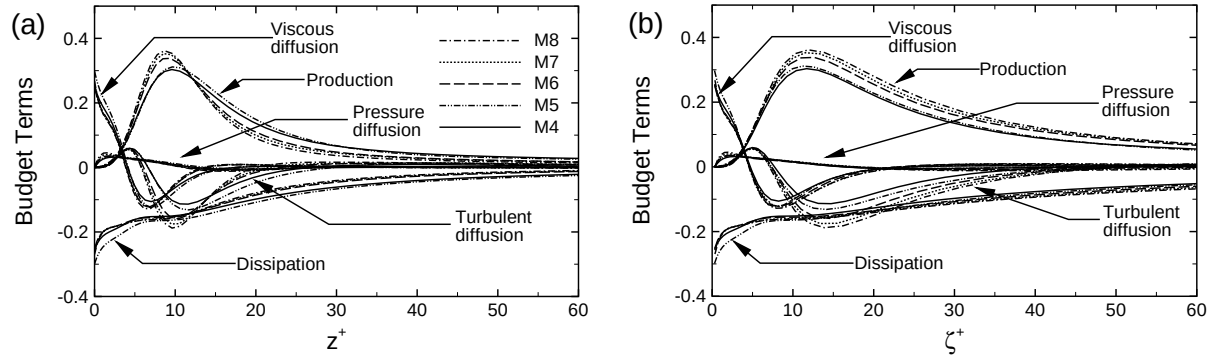

(a) (b)

Figure 12. Turbulent Kinetic Energy budgets for the Mach number varying cases. (*a*) Plotted against z^+ and *b*) plotted against ζ^+.

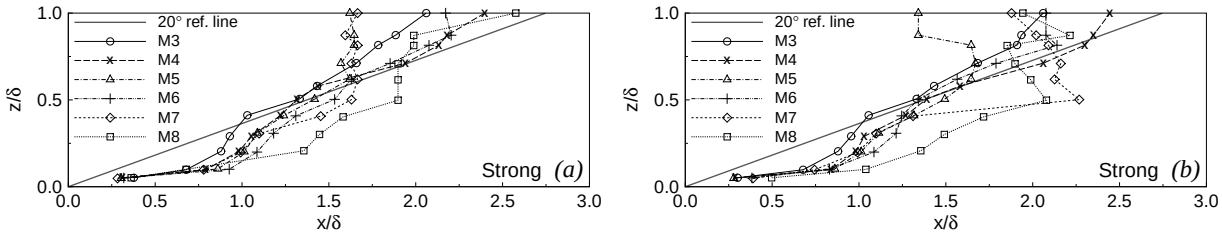

Figure 13. Packet geometries defined by the 'strong' correlations of τ_w and ρu. (*a*) Using the correlations only, per the method of Brown and Thomas.[1] (*b*) Using the correlations with the condition that a 'geometric event' at the wall is present.

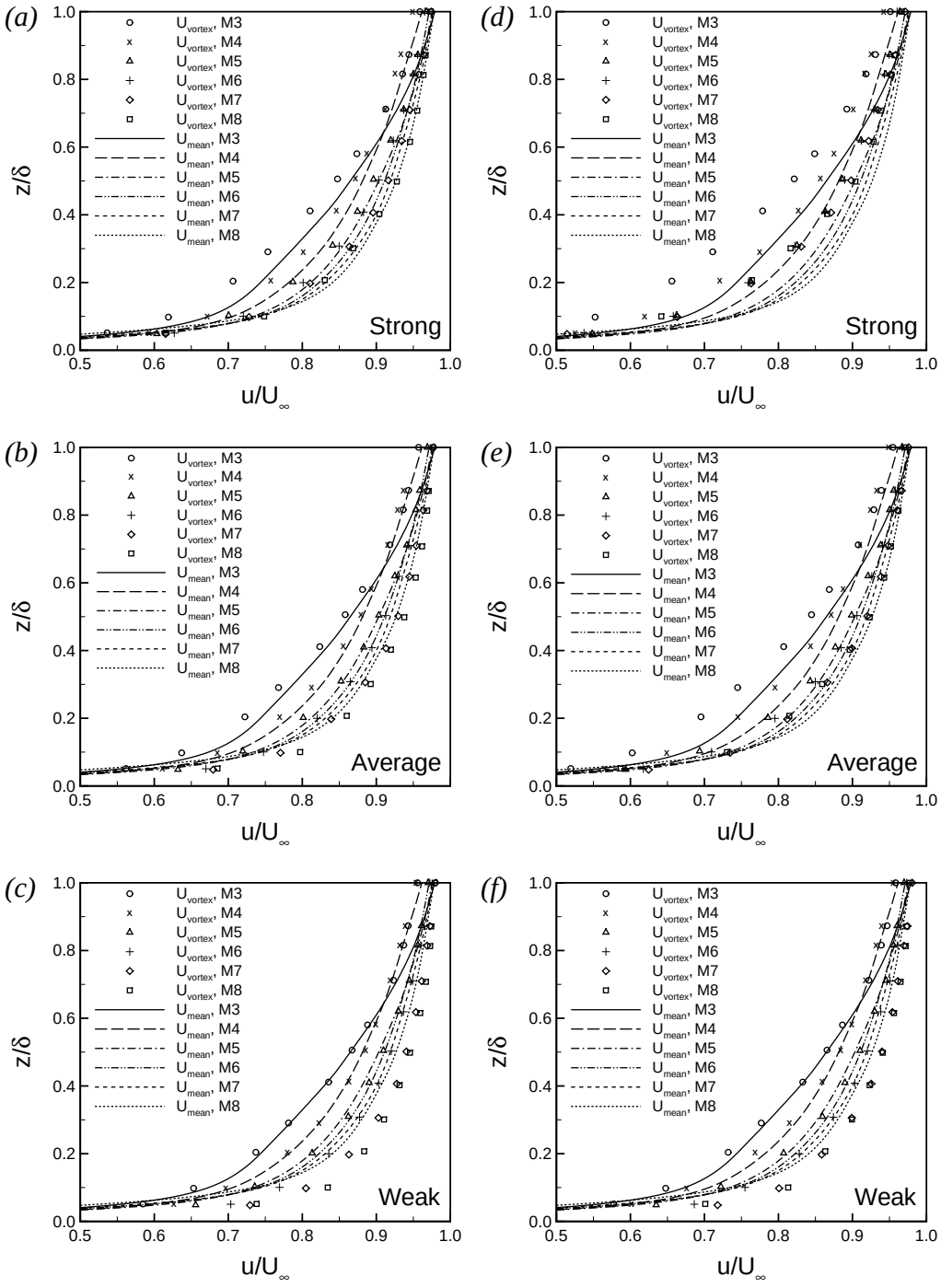

Figure 14. Average vortex convection velocity versus distance from the wall computed using the 'strong,' 'average,' and 'weak' correlations of τ_w and ρu. (*a–c*) Using the correlations only, per the method of Brown and Thomas.[1] (*d–f*) Using the correlations with the condition that a 'geometric event' at the wall is present.

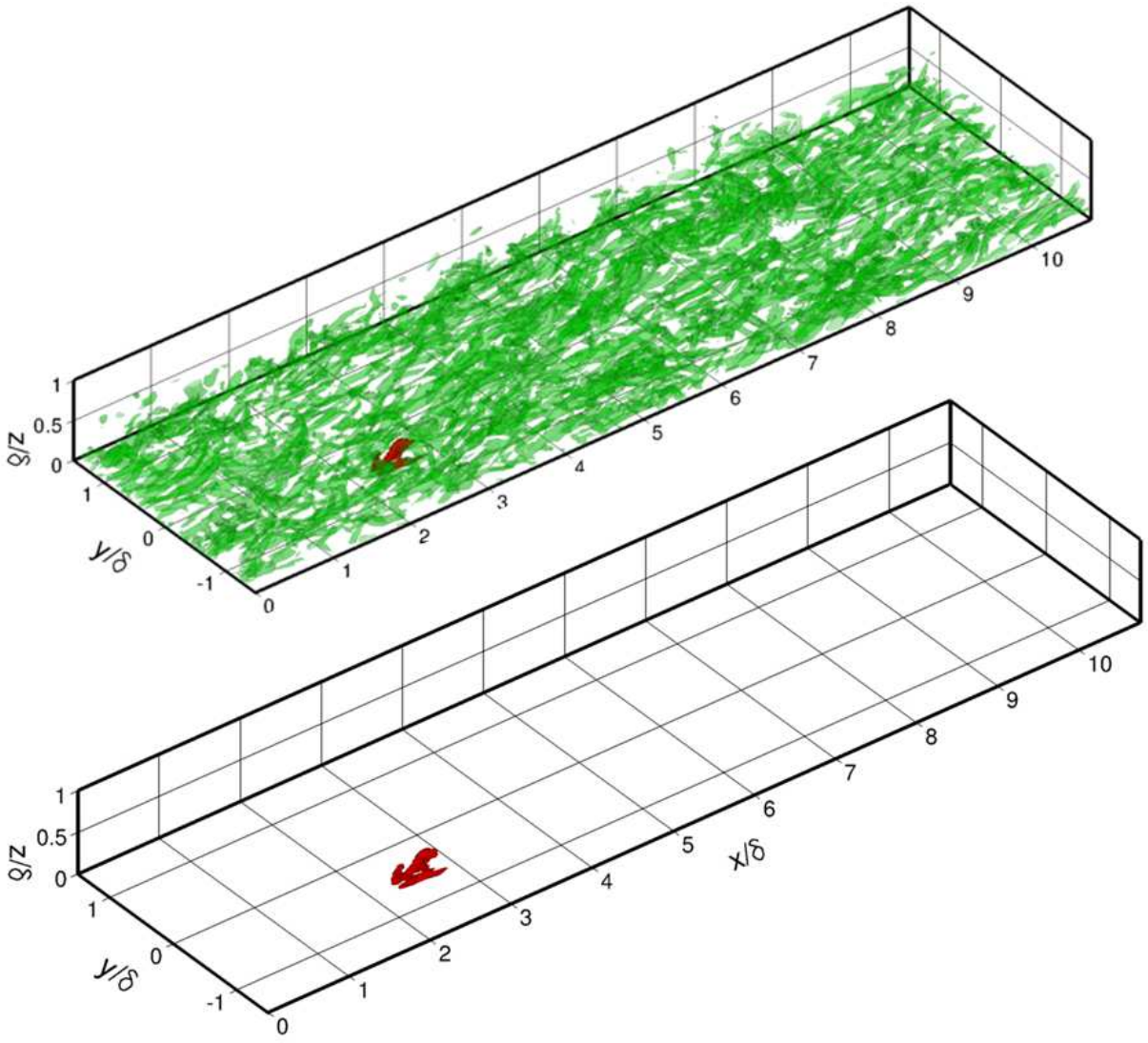

Figure 15. A hairpin packet in a Mach 8 boundary layer colored in red. Structures are visualized by an iso-surface of swirl at $4.5\overline{\lambda_{ci}}$. This packet is subsequently tracked and its wall signatures are identified below in Figures 16 and 17.

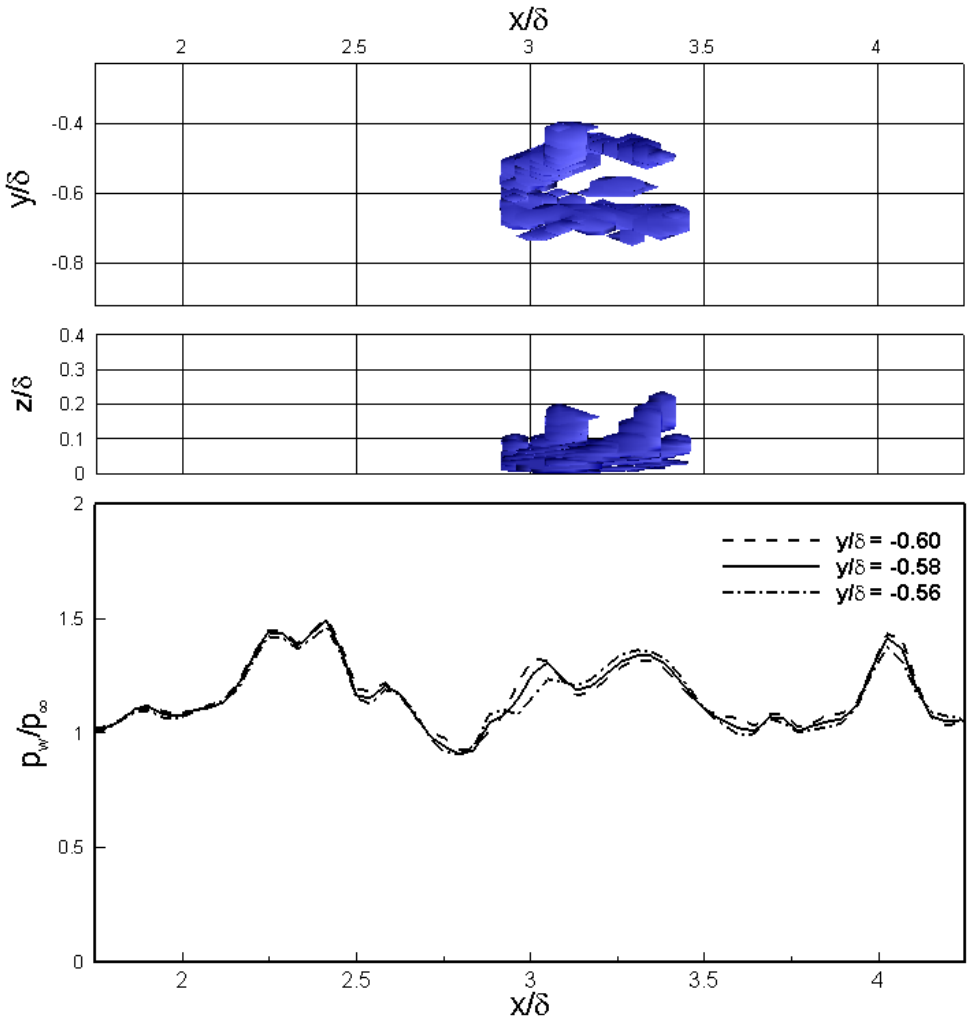

Figure 16. Wall-pressure signature of a hairpin packet in DNS of Mach 8 boundary layer. The top and middle part of the figure show the vortical structure, visualized by an iso-surface of swirl (the threshold is $4.5\overline{\lambda_{ci}}$). The top part of the figure shows a streamwise-spanwise plane, and the middle part shows a streamwise-wall normal plane. The bottom part of the figure plots the wall-pressure along three different streamwise lines.

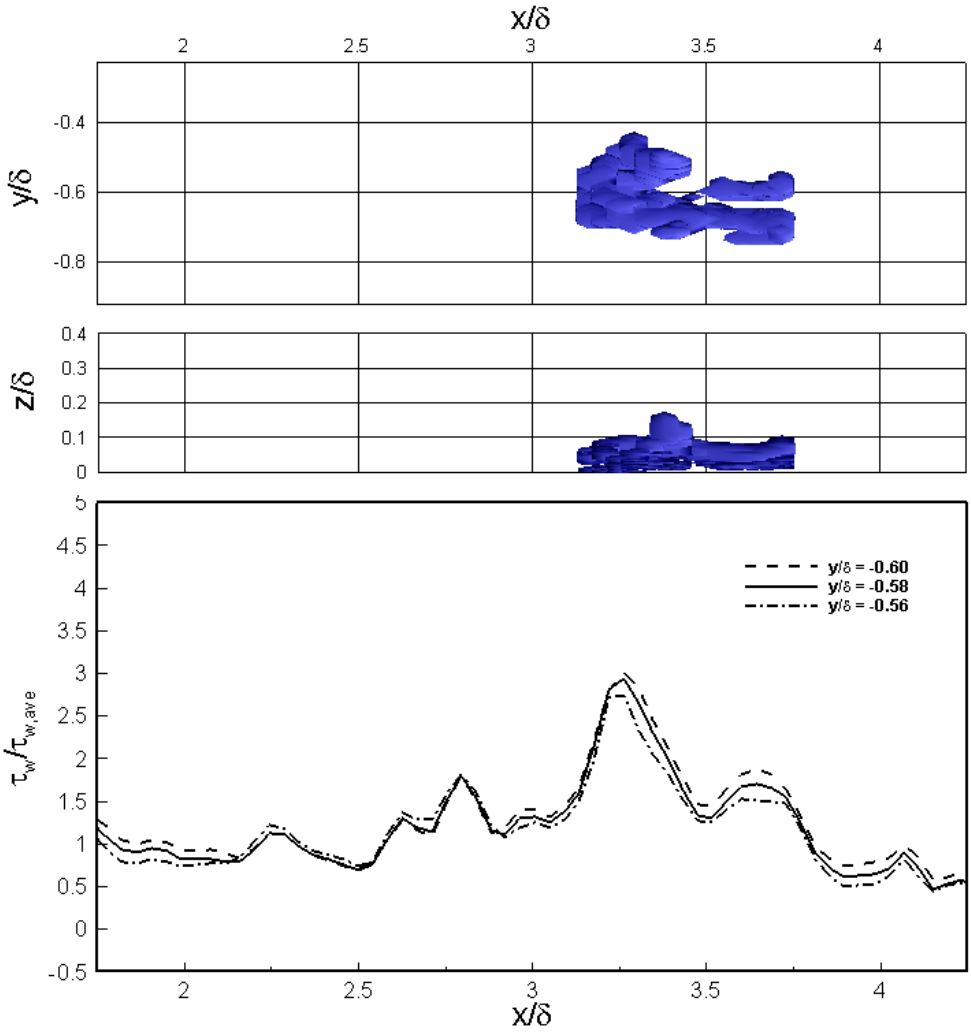

Figure 17. As in figure 16 above, except that the wall-shear stress signature is shown.